applied sciences

MDPI

Article

Furfural Hydrogenation on Modified Niobia

Andrea Jouve [1], Stefano Cattaneo [1], Daniel Delgado [2], Nicola Scotti [3], Claudio Evangelisti [4], José M. López Nieto [2] and Laura Prati [1,*]

1 Dipartimento di Chimica, Università degli Studi di Milano, Via Golgi 19, I-20133 Milano, Italy; andrea.jouve@unimi.it (A.J.); stefano.cattaneo2@unimi.it (S.C.)
2 Instituto de Tecnología Química (UPV-CSIC), Universitat Politècnica de València-Consejo Superior de Investigaciones Científicas, Avenida de los Naranjos s/n, 46022 Valencia, Spain; dadelmuo@itq.upv.es (D.D.); jmlopez@itq.upv.es (J.M.L.N.)
3 CNR, Institute of Molecular Science and Technologies (ISTM), Via Golgi 19, I-20133 Milan, Italy; nicola.scotti@istm.cnr.it
4 CNR, Institute of Molecular Science and Technologies (ISTM), Via G. Fantoli 16/15, 20138 Milan, Italy; claudio.evangelisti@istm.cnr.it
* Correspondence: laura.prati@unimi.it; Tel.: +39-0250-314-357

Received: 1 May 2019; Accepted: 30 May 2019; Published: 3 June 2019

Abstract: In this study, niobia-based materials have been used as supports for Pt nanoparticles and used in the hydrogenation of furfural. The incorporation of dopants (W^{6+} and Ti^{4+}) in the Nb_2O_5 structure induced modifications in the surface acidity of the support; in particular, the addition of W^{6+} increased the amount of Lewis acid sites, while the addition of Ti^{4+} decreased the number of Lewis acid sites. As a result, the catalytic activity towards the hydrogenation of furfural was affected; high surface acidity resulted in high catalytic activity. The selectivity of the reaction changed with the support acidity as well, with higher amount of furfuryl alcohol produced decreasing the Lewis acid sites.

Keywords: platinum; niobia; niobium oxide; furfural; hydrogenation; furfuryl alcohol; pentanediol; Lewis acid

1. Introduction

Over the last decade the depletion of fossil fuel reserves, combined with the environmental crisis, has led scientists to focus their attention on the production of chemicals and fuels in a greener and more sustainable way. In this respect, biomass is playing a crucial role, since it is the most attractive carbon feedstock due to its abundancy and low production cost [1–4]. Lignocellulose (non-edible plant-based biomass), in particular, is composed of cellulose, hemicelluloses and lignin; all together they represent ca. the 75% of the 170 billion metric tons of the total biomass production per year by photosynthesis [5]. The hydrolysis process of hemicellulose leads to a homogeneous mixture of pentoses and hexoses, such as xylose, arabinose, glucose, mannose and galactose [6–9]. The further dehydration of pentoses generates furfural, a potential chemical platform for the synthesis of several chemicals and biofuels [10,11]. Furfural can also be produced directly from cascade hydrolysis and dehydration of hemicellulose; in this respect, solid acid catalysts are typically used in biphasic solvent systems in order to promote the process [12,13]. The use of solid acid catalysts has been recently studied in the conversion of furfural into high-added value products (Figure 1) [14,15]. The presence of Brønsted and/or Lewis acid sites, in fact, can change both the activity and selectivity of the reaction. Bui et al., for example, reported a domino reaction catalyzed by zeolites with both Brønsted and Lewis acid sites for the production of γ-valerolactone, where Lewis sites catalyzed the hydrogenation step, while the Brønsted sites catalyzed the ring-opening hydration step [16]. Lewis acidity is responsible

for acetalization reactions as well, as reported by Taylor and co-workers, who observed considerable amount of furfuraldehyde diethyl/dimethyl acetal during the hydrogenation of furfural to furfuryl alcohol over Pt nanoparticles supported on various metal oxides (γ-Al_2O_3, CeO_2, SiO_2, and ZnO) in alcoholic solvent (either ethanol or methanol) [17]. It is therefore clear that the reaction pathway can be altered through a careful tuning of the acidic properties of the heterogeneous catalysts used as well as the solvent employed.

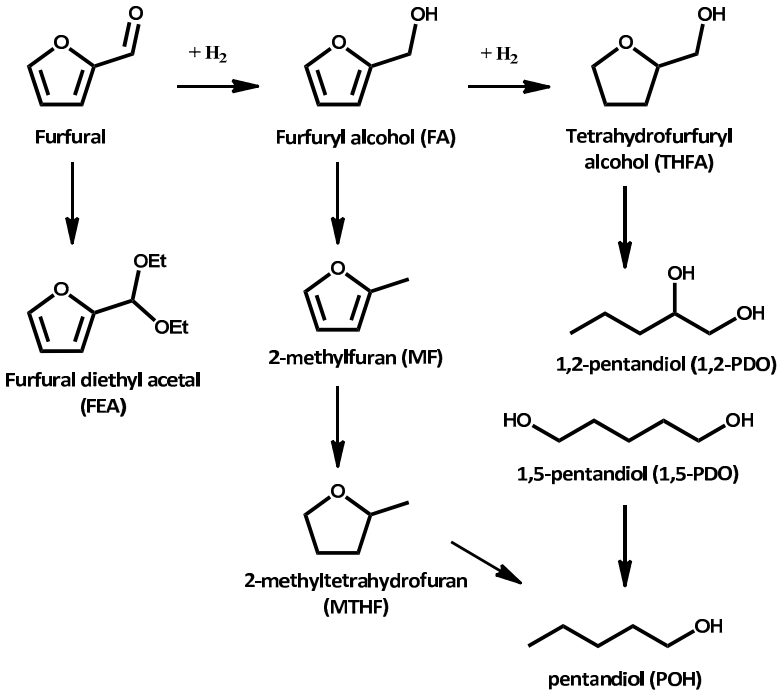

Figure 1. Reaction scheme of the furfural hydrogenation reaction.

One of the most important solid acid catalyst is niobia (Nb_2O_5, niobium oxide). Niobia is a metal oxide showing NbO_6 octahedra, with a great structural versatility [18,19]. The presence of Nb=O bonds in the Nb_2O_5 structure is in fact associated with Lewis acid sites, while the highly polarised Nb-O bonds generate surface OH groups which function as Brønsted acid sites [19–21]. This intrinsic acidity, combined with air-stability and water-insolubility, makes niobia a suitable catalyst for reactions in aqueous and polar media and therefore a very attractive material for industrial use [22,23]. Niobia-based catalysts have in fact been extensively studied for the aforementioned hydrolysis and dehydration of hemicellulose to furfural [14,23]. However, deactivation phenomena are often reported in these reactions and it is generally attributed to the strong acid nature of the niobia active sites; acid-catalyzed formation of solid products such as coke and humins, in fact, can partially cover the active sites and therefore substantially decrease the overall catalytic activity [23–25].

One of the most common methods to finely tune the surface acidity of niobia is the addition of a second metal oxide, which can result in the formation of new materials with different chemical and physical features in comparison with the starting materials. Several techniques can be employed in order to obtain the so-called niobia-based mixed oxides, such as hydrothermal synthesis, sol-gel, and co-precipitation techniques [26–31]. Nb_2O_5-MeO_2 (Me = Zr, Ce and Ti) mesoporous mixed oxide were, for example, prepared by Auroux et al. by evaporation-induced self-assembly and applied in the dehydration of fructose [32]. The synthesised catalysts showed acid properties dependent on the nature of the oxide that was mixed with niobia; moreover, both activity and selectivity showed dependence on the amount of surface strong acid sites.

Another interesting way to finely modulate the surface acidity of niobia is by introducing a second metal into the Nb_2O_5 structure. This procedure is called ion doping and it has been successfully

applied in the production of several metal-doped Nb_2O_5. Marzo et al., for example, prepared K-, Ba-, and Nd- doped niobia and tested in the fructose dehydration reaction [24]. The authors showed decreased deactivation phenomena due to the doping of niobia with basic species; these basic species affected only the strong acid sites where humin is formed, while fructose dehydration proceeded with good stability on the lower acid sites.

The activity and selectivity of niobia-based catalysts can be further improved by deposition of active metal nanoparticles on its surface. These bifunctional catalysts are especially employed in specific reactions, where acid sites provide the active centre for dehydration reactions and the metal nanoparticles provide the catalytic centre for other reactions to occur, such as oxidations or hydrogenations [33]. Moreover, the interaction between the adsorbed metal nanoparticles and the niobia surface can significantly alter the electronic density on the surface of the nanoparticles, leading to a different interaction between the active metal site and the substrates/products [34].

Despite its unique properties, however, Nb_2O_5 has not received as much attention as support for metal nanoparticles like many other metal oxides (i.e., TiO_2, Al_2O_3, SiO_2, and CeO_2). In this work, Nb_2O_5 and metal-doped Nb_2O_5 (W-Nb_2O_5 and Ti-Nb_2O_5) with different surface acidity were synthesised by hydrothermal synthesis. The four materials were then used as support for Pt nanoparticles and the catalysts tested in the hydrogenation of furfural. In-depth characterization, such as electron microscopy analysis, X-ray Diffraction, Raman spectroscopy, and Infrared studies by pyridine adsorption has been carried out on the catalysts in order to fully understand their physical-chemical properties.

2. Materials and Methods

2.1. Support Preparation

Nb_2O_5 and metal-doped Nb_2O_5 supports (W-Nb_2O_5 and Ti-Nb_2O_5) were prepared by hydrothermal synthesis. For the synthesis of Nb_2O_5, 11.15 g of niobium oxalate (abcr, Karlsruhe, Germany, 99.95%) were dissolved in 24 g of MilliQ water and kept under stirring at 80 °C for 10 min. The mixture was then kept for 2 days in a sealed autoclave at 175 °C. The solid obtained was filtered, washed with 500 mL of deionized water, and dried at 100 °C for 16 h. Finally, the material was heat-treated in N_2 at 550 °C for 2 h, with a heating rate of 3 °C min^{-1} under a nitrogen flow of 30 mL·min^{-1}.

For the synthesis of metal-doped Nb_2O_5, the following metal precursors were used: titanium(IV) oxysulfate—sulphuric acid hydrate (Sigma-Aldrich, Haverhill, MA, USA, 99.95%) and ammonium metatungstate hydrate (Sigma-Aldrich, 99.99%). 10.04 g of niobium oxalate were dissolved in 19 g of MilliQ water and kept under stirring at 80 °C for 10 min. At the same time, the appropriate amount of dopant precursor (Nb:metal molar ratio of 9:1; 0.66 g of titanium(IV) oxysulfate or 0.59 g of ammonium metatungstate) was dissolved in 5 mL of MilliQ water and kept under stirring at 80 °C for 10 min. The dopant mixture was added to the niobium precursor solution and kept under stirring for an additional 10 min at 80 °C. As per the synthesis of pure niobia, the resulting mixture was kept at 175 °C for 2 days in a sealed autoclave. The support was then filtered, washed thoroughly with 500 mL of deionized water, and dried for 16 h at 100 °C. Finally, the metal-doped niobia supports were heat-treated for 2 h at 550 °C with a heating rate of 3 °C·min^{-1} under a nitrogen flow of 30 mL·min^{-1}.

2.2. Catalysts Preparation

The Pt nanoparticles supported onto niobium oxide-based support were synthesized by the Metal Vapor Synthesis (MVS) technique following previously reported procedure [35]. Platinum vapors generated at 10^{-5} mbar by resistive heating of a tungsten wire surface coated with electrodeposited platinum (ca. 103.0 mg) were co-condensed with mesitylene (100 mL, Sigma-Aldrich, 98%) in a glass reactor at −196 °C. The reactor chamber was heated to the melting point of the solid matrix and the resulting brown solution (95 mL) was kept under argon atmosphere in a Schlenk tube at −40 °C. The Pt-content of the obtained Pt solvated metal atoms (SMA) was determined by ICP-OES (0.8 mg_{Pt}/mL). The Pt/mesitylene SMA (2.5 mL of Pt/mesitylene, 2 mg Pt) was added to a dispersion of the support

(200 mg) in mesitylene (5 mL). The resulting suspension was warmed up to 25 °C under stirring for 6 h. Afterwards the solvent was removed by vacuum and the obtained solids Pt/Nb_2O_5, Pt/W-Nb_2O_5, and Pt/Ti-Nb_2O_5 were washed with *n*-pentane (Sigma-Aldrich, 99%) and dried under reduced pressure. All isolated samples contained 1.0 wt% of Pt as determined by Inductively Coupled Plasma-Optical Emission Spectrometry (ICP-OES) analysis.

2.3. Catalysts Characterisation

Transmission electron microscopy (TEM) analysis of the supported Pt-NPs was carried out with a ZEISS LIBRA 200FE microscope equipped with a 200 kV FEG source. The specimens were finely smashed in an agate mortar, suspended in isopropanol (Sigma-Aldrich, 99.8%) and sonicated, then each suspension was dropped onto a lacey carbon-coated copper grid (300 mesh) and the solvent was evaporated. Histograms of the particle size distribution were obtained by counting at least 500 particles. The mean particle diameter (dm) was calculated using the formula $dm = \sum d_i n_i / \sum n_i$, where n_i is the number of particles with diameter d_i.

Scanning electron microscopy analyses were performed in a JEOL JSM 6300 LINK ISIS microscope equipped with an Oxford LINK ISIS System to carry out compositional analysis by Energy-Dispersive X-ray Spectroscopy (XEDS).

N_2-adsorption experiments were carried out in a Micromeritics ASAP 2000 instrument. Specific surface areas were determined from N_2 adsorption isotherms by means of Brunauer–Emmett–Teller (BET) method. The samples were degassed under vacuum at 400 °C prior to N_2 adsorption.

Inductively Coupled Plasma-Optical Emission Spectrometry (ICP-OES) was carried out with an iCAP 6200 Duo upgrade, Thermofisher instrument. A sample (0.5 mL) of Pt-SMA was heated over a heating plate in a porcelain crucible in the presence of aqua regia (2.0 mL) three times followed by dissolving the solid residue in 0.5 M aqueous HCl. The limit of detection calculated for platinum was 2 ppb.

Powder X-ray diffraction patterns were collected in a PANalytical X'pert PRO diffractometer with an X´Celerator detector, using a monochromatic Cu Kα_1 as X-rays source. Diffractograms were recorded with the detector arranged in a Bragg-Brentano geometry.

Raman spectra were recorded in an inVia Renishaw spectrometer equipped with a Renishaw HPNIR laser and an Olympus microscope. The measurements were carried out at an exciting wavelength of 514 nm and an approximate power on the sample of 15 mW.

Fourier Transform Infrared (FT-IR) studies by pyridine adsorption and desorption were performed on a FTS-60 spectrophotometer equipped with a mid-IR MCT detector (BioRad). Before the analysis, the sample disk (10−20 mg) was dehydrated at 75 °C for 40 min under vacuum, then one spectrum was collected before probe molecule adsorption, as a blank experiment. Next, pyridine (Sigma-Aldrich, 99.8%) adsorption was carried out at room temperature and the following desorption steps were run for 30 min at various temperature (from room temperature to 250 °C). All spectra were recorded at room temperature. The determination of the amount of adsorbed pyridine ($mmol_{Py}/g_{cat}$) was performed according to the procedure reported by Emeis [36] on the spectra registered at 150 °C.

2.4. Catalytic Hydrogenation Reactions

Furfural hydrogenation reactions were carried out in a 100 mL stainless steel autoclave equipped with a glass inlet. In a typical experiment, 10 mL of a 0.1 mol L^{-1} solution of furfural (Sigma-Aldrich, 99%) in ethanol (Sigma-Aldrich, 99.8%) and an appropriate amount of catalyst (furfural:Pt molar ratio of 1:500) were placed into the glass inlet along with a magnetic stirrer. The autoclave was sealed and flushed several times with N_2 first in order to remove any residual oxygen in the atmosphere and then pressurized with 7 bar of H_2. The autoclave was then heated up to the desired temperature (50 °C) and the reaction mixture stirred at a constant stirring rate of 1200 rpm. Samplings were carried out by stopping the stirring and quenching of the reaction under cold water. 300 µL of reaction mixture were withdrawn and centrifuged in order to separate the catalyst. 100 µL of the supernatant solution

were then diluted with a solution of an external standard (dodecanol, Sigma-Aldrich, 98%) for GC measurement. Product analysis was carried out with a GC-MS (Thermo Scientific, Waltham, MA, USA, ISQ QD equipped with an Agilent VF-5ms column) and the resulting fragmentation peaks were compared with standards present in the software database. Product quantification was carried out through a GC-FID equipped with a non-polar column (Thermo Scientific, TRACE 1300 equipped with an Agilent HP-5 column).

3. Results

3.1. Catalysts Characterisation

SEM-EDX analyses were performed on the metal-doped niobia supports (Figure 2) in order to calculate the effective loading of the dopant into the niobia structure. The two supports show similar dopant loading very close to the nominal value of 10 at% (Table 1).

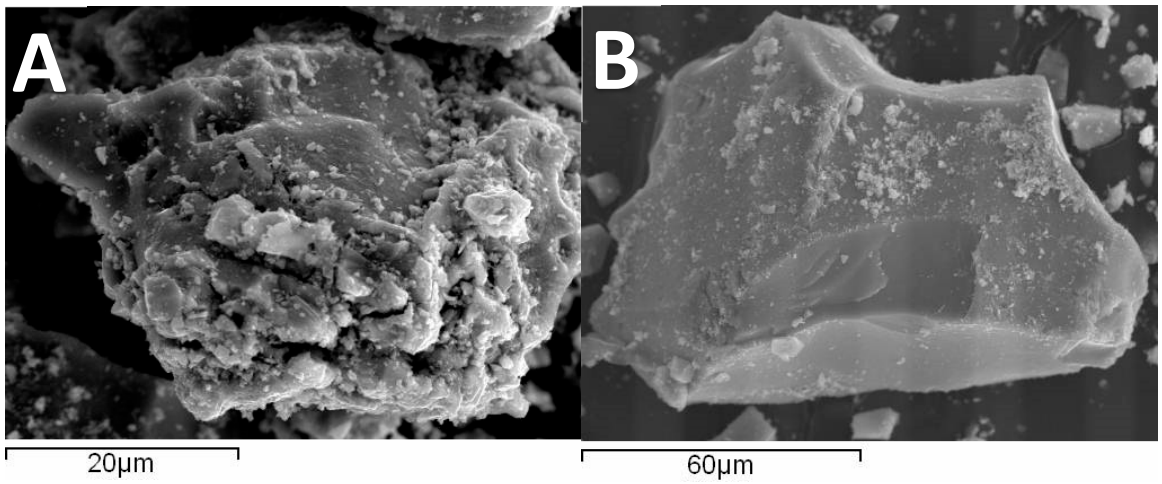

Figure 2. Representative scanning electron microscopy (SEM) images of (**A**) Ti-Nb_2O_5 and (**B**) W-Nb_2O_3.

Table 1. Dopant loading on the niobia based supports by Energy-Dispersive X-ray Spectroscopy.

Support	Dopant [at%]
Ti-Nb_2O_5	9.68
W-Nb_2O_5	9.35

Pt have been deposited onto the niobium oxide-based supports by MVS following the procedure previously used for other kind of supports [35,37,38]. TEM micrographs collected on the three samples (Figure 3) revealed the niobium oxide-based supports densely populated by monodispersed Pt nanoparticles with very small particle sizes, ranging mainly 1.0–1.5 nm, regardless of the support used.

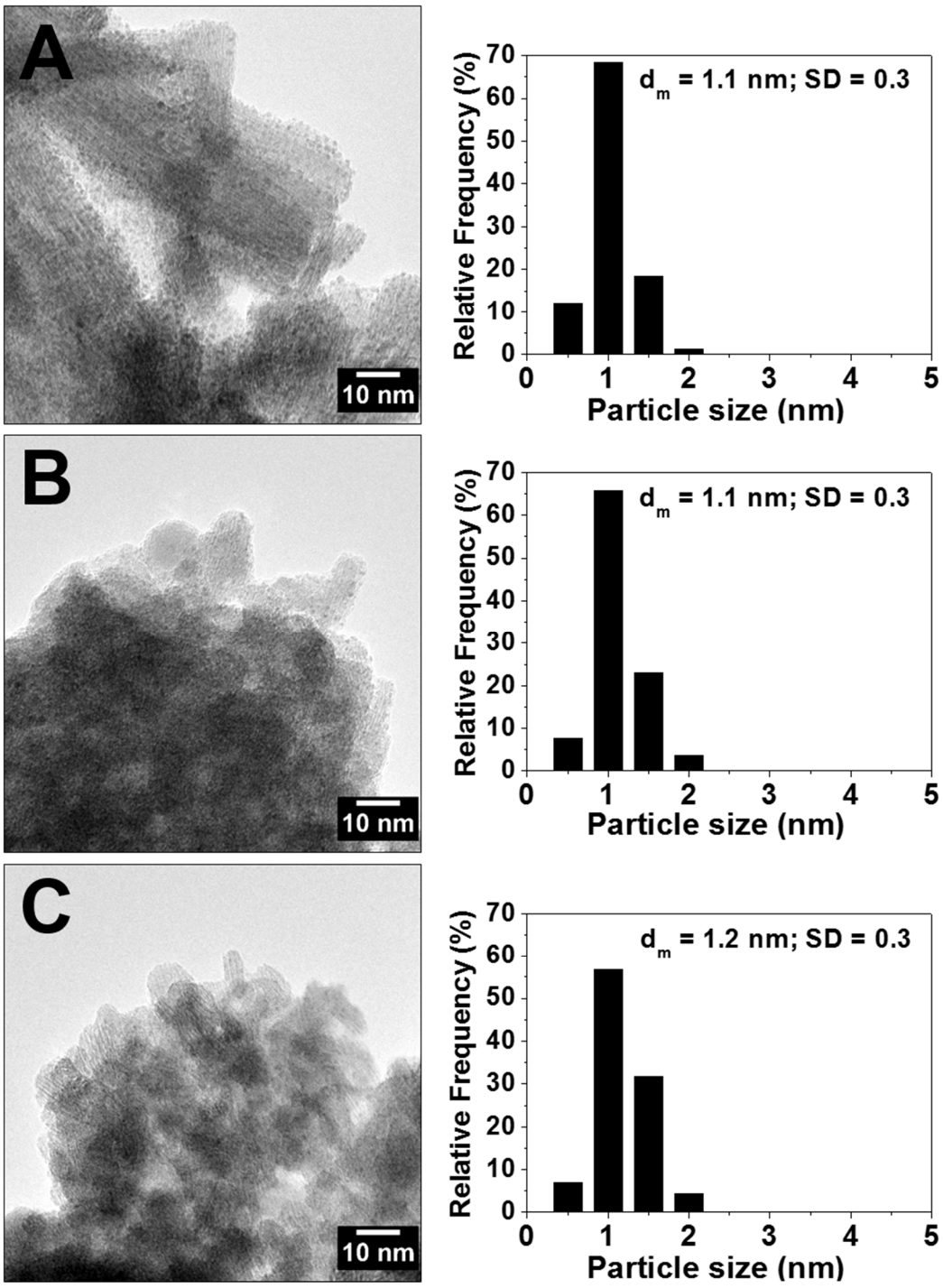

Figure 3. Representative Transmission Electron Microscopy (TEM) micrograph (315,000 X) and histogram of Pt particle size distribution of the Pt/Nb_2O_5 (**A**), Pt/Ti-Nb_2O_5 (**B**) and Pt/W-Nb_2O_5 (**C**) sample.

Figure 4 depicts XRD patterns of niobia-based supports. All the materials only show two well-defined diffraction maxima at 2θ values of ca. 23 and 46° (Figure 4A). Those signals can be ascribed to 001 and 002 planes in any ReO_3-type related structure, and are assigned to a well-ordered vertex-sharing octahedra along one direction, showing an opposite vertex distance of ca. 3.8 Å [39,40]. The rest of the observed signals show a broad profile, indicating the amorphous nature of the *ab*-plane of the structure in all cases. Accordingly, it becomes difficult to ascribe the distribution of the atoms along *a* and *b* directions to a specific polymorph. Nevertheless, we can estimate the partial substitution

of Nb by the dopants by analyzing the shifts in 2θ of the abovementioned 001 signal. Analyzed *c*-parameter values, calculated from 2θ values of 001 signal by using Bragg equation are summarized in Table 2. It can be seen that the incorporation of Ti^{4+} into Nb_2O_5 framework leads to a decrease in the *c*-parameter, from 3.89 Å to 3.80 Å, which is in line with ionic radius of Nb^{5+} and Ti^{4+} (0.64 and 0.60 Å, respectively) [41]. On the other hand, when $W^{6+/5+}$ is used as promoters, *c*-parameter slightly increases up to 3.90 Å (Table 2).

When dealing with these pseudocrystalline materials (i.e., with a well-ordered structure just along one crystallographic direction), the demonstration of the partial substitution of Nb by XRD is not so direct. In this sense, the variation of cell parameters can present opposite trends, i.e., the isomorphic substitution in the crystal framework can derive in an increase of the dimensions of the unit cell in some specific directions, while showing decreasing trends in others. This has been observed in the partial substitution of W for Mo in tetragonal tungsten bronze-based materials [42]. HR-TEM analysis on Pt nanoparticles dispersed on the niobia-based oxides (Figure S1) confirmed the presence of a pseudocrystalline phase of the supports. All of them appeared to be constituted by primary nano-domains, 7–20 nm long and 4–10 nm in width stacked on each other, mainly along their length, to form agglomerates. According to the XRD results, the direction of elongation of the domains was found to be coincident with the [001] direction, coincident with the c-axis of the lattice.

In order to shed some light on this issue, we have analyzed Nb_2O_5-based supports by Raman spectroscopy (Figure 4B). In this case, the incorporation of $W^{6+/5+}$ or Ti^{4+} within Nb_2O_5 framework should promote variations on the nature of metal–oxygen bonds with respect to the undoped material. Undoped Nb_2O_5 displays a broad Raman feature centred at 706 cm^{-1}, that can be assigned to symmetric stretching modes of Nb-O in distorted octahedra (Figure 4B, spectrum (*a*) [43]. Interestingly, the incorporation of a second element gives rise to frequency shifts to: (i) higher frequencies, like in the case of W-containing Nb_2O_5 (719 cm^{-1}) (Figure 4B, spectra (*b*); (ii) lower frequencies, for Ti-containing catalyst (694 cm^{-1}) (Figure 4B, spectrum *c*). The shift can be explained in terms of the specific weight of the dopant elements, i.e., heavier species (like W^{6+}) will shift the bands to higher frequencies, while lighter dopants (like Ti^{4+}) would shift the bands to lower frequencies. In addition, doped supports show broader Raman signals, due to a higher disordered degree (as observed in XRD patterns) [44]. In turn, signals corresponding to TiO_2 and WO_3 oxides were always absent in the supports. All these observations suggest either an effective interaction of the promoter with Nb_2O_5, or the incorporation of the dopants in framework positions.

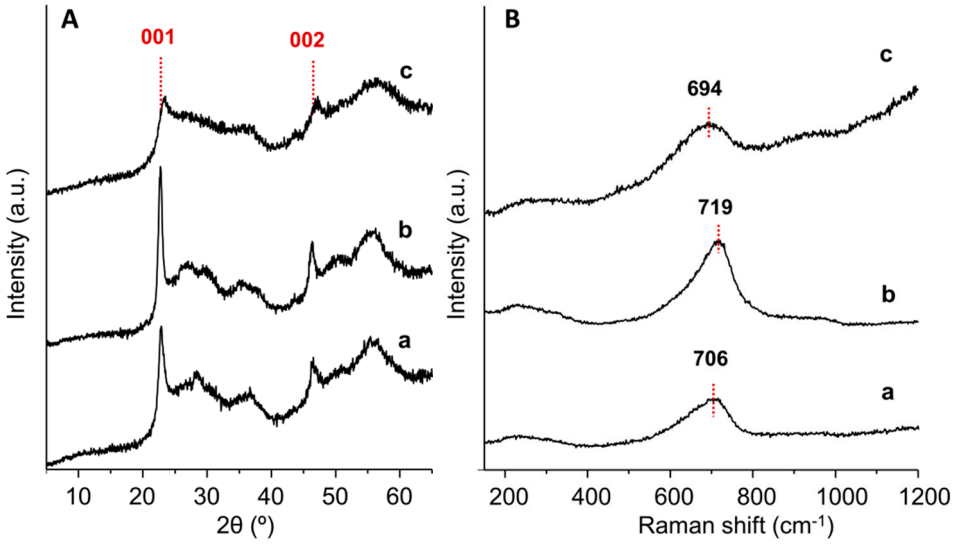

Figure 4. X-ray diffraction (XRD) patterns (**A**) and Raman Spectra (**B**) of Nb_2O_5-based supports: (a) Nb_2O_5; (b) W-Nb_2O_5; (c) Ti-Nb_2O_5.

Table 2. Surface area and c-parameter of the different supports used.

Support	Surface Area (m^2 g^{-1})	c-Parameter (Å) [a]
Nb_2O_5	95	3.89
W-Nb_2O_5	130	3.90
Ti-Nb_2O_5	35	3.80

[a] Determined by Bragg equation from X-ray diffraction (XRD) patterns, using 2θ values of 001 peak.

BET analyses were carried out on the pure supports in order to evaluate differences in surface area (Table 2). Upon inclusion of W to the niobia lattice, the surface area increased from 95 to 130 $m^2 \cdot g^{-1}$ (Nb_2O_5 and W-Nb_2O_5 respectively). On the other hand, the addition of Ti had the opposite effect and the surface area decreased to 35 $m^2 \cdot g^{-1}$.

The adsorption of basic probe molecules followed by IR analysis is a common technique used to investigate the surface acidity of solid catalysts. Here IR analysis of adsorbed pyridine (Py) has been performed. As reported in the literature, the contact with the amine gives rite to several bands in the range of 1400–1700 cm^{-1}, depending on the type of the interaction between pyridine and catalyst surface (physisorbed pyridine, Lewis acid sites, Brønsted acid sites). A weak interaction between the catalyst and the probe molecule, resulting from very weak or no acidity (physisorption or hydrogen bonding), gives rise to an adsorption band in the range of 1440–1450 cm^{-1} and another one at 1580–1600 cm^{-1}. These bands easily decrease with the temperature and over 100 °C physisorbed pyridine could be considered fully desorbed. When pyridine is interacting with Lewis acid site, two main absorption peaks are detected: one centered at ca. 1450 cm^{-1} (ν_{19b} mode) and a second centered at ca. 1610 cm^{-1} (ν_{8a} mode). In the case of Lewis acidity also a small band at 1580 cm^{-1} could be observed. On the other hand, in presence of Brønsted acid sites, a proton transfer occurs to form the pyridinuim ion though the protonation of pyridine. This results in a band at 1550 cm^{-1} (ν_{19b} mode), followed by a band near 1640 cm^{-1} (ν_{8a} mode). Also a band at ca. 1490 cm^{-1} is usually detected, but it was not unambiguously assigned to a specific acid site, being identified as the result of either kind of interactions. Importantly, pyridine on both Lewis and Brønsted sites is resistant to outgassing with bands that could be detected also at high temperature [45–47].

In Figure 5 we reported the FT-IR spectra of pyridine recorded after degassing at 150 °C for the investigated materials. All the catalysts exhibit the bands pattern typical for Lewis acids sites, with the bands at 1448 cm^{-1} and 1609 cm^{-1} (and the small one at 1576 cm^{-1}), whereas Brønsted sites are absent. Nb_2O_5 is well known to feature mainly Lewis acidity, while some structural modifications (e.g., the introduction of phosphate groups) could generate Brønsted sites, although this is not the case [48,49].

It is very important to highlight that the samples differ significantly for the intensity of the bands, thus indicating a strong difference in terms of acid sites concentration. Indeed, the quantitative determination of adsorbed pyridine ($mmol_{Py}/g_{cat,}$ Table 3), made on the basis of band located at 1448 cm^{-1} according to the procedure reported by Emeis et al. [36], shows that Pt/Ti-Nb_2O_5 possesses a small acidity compared with the parent Pt/Nb_2O_5, while the modification with W drastically increases the acid site concentration of the final Pt/W-Nb_2O_5. In the Nb-based materials the Lewis acidity is generated by the unsaturated Nb(V) sites [48,49]: here it appears that the introduction of W in the Nb_2O_5 structure enhances the Lewis character of the solid, whereas Ti drastically affects this features, while Brønsted sites are never observed.

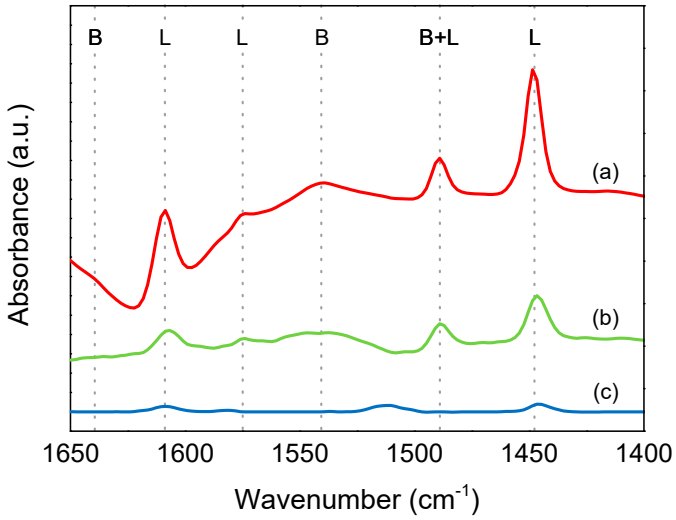

Figure 5. Fourier-transform infrared (FT-IR) spectra of pyridine recorded after evacuation at 150 °C (L = Lewis acid site band; B = Brønsted acid sites band) and normalised by the disk weight. (a) Pt/W-Nb_2O_5, (b) Pt/Nb_2O_5 and (c) Pt/Ti-Nb_2O_5.

Table 3. Amount of adsorbed pyridine on Lewis site.

Catalyst	$mmol_{Py}/g_{CAT}$
Pt/Nb_2O_5	0.078
Pt/W-Nb_2O_5	0.191
Pt/Ti-Nb_2O_5	0.014

3.2. Catalytic Results

Depending on the reaction conditions and the catalysts used, the hydrogenation of furfural can proceed in different directions: products of carbonyl hydrogenation, ring hydrogenation, ring opening, etherification, hydrodeoxygenation, and decarboxylation have been reported in literature (Figure 1). Furfural hydrogenation reactions were carried out in this study at 50 °C and 5 bar of H_2, using ethanol as solvent. Typically, under this mild reaction conditions, furfuryl alcohol (FA) and tetrahydrofurfuryl alcohol (THFA) are reported to be the main products, as a result of the hydrogenation of the carbonyl group and the furan ring (Figure 1).

Figure 6 shows the reaction profile of the furfural hydrogenation reaction carried out using Pt/Nb_2O_5 as catalyst. After 15 min, almost half of the starting substrate was converted (42%) and the main products were furfural diethyl acetal (FEA) and FA (44 and 43% of selectivity respectively), with low amount of THFA being produced as well (7%). The presence of the acetal is not surprising, since it is often reported when the reaction is carried out with solid acid catalysts in low-chain alcoholic solvents (i.e., ethanol). Furfural was fully converted after 1 h and both FA and FEA were transformed. The FA reached a maximum after 30 min of reaction (52%) and then decreased, with a consequent increase of THFA (31% of selectivity after 2 h), whereas FEA decreased over time, with no trace of acetal remained after 2 h. Interestingly, products of hydrogenolysis (ring-opening and hydrodeoxygenation) such as 1,2-pentanediol (1,2-PDO), 1,5-pentanediol (1,5-PDO), and1-pentanol (POH) were present in significant amounts in the final reaction mixture. In particular, 1,2-PDO and 1,5-PDO (9 and 13% of selectivity respectively after 2 h) are generated from the hydrogenolysis of the C-O bond in the THFA ring, while POH (11% of selectivity after 2 h) can either derive from the hydrodeoxygenation of 1,2-PDO and 1,5-PDO or from the hydrodeoxygenation of THFA and successive hydrogenolysis of the C-O bond. Only small amount of 2-methylfuran (MF) and 2-methyltetrahydrofuran (MTHF) were detected at any point of the reaction (less than 5% in total) along with other acetalization products (such as tetrahydrofurfural dietyl acetal and 5-hydroxypentanal diethyl acetal, hereafter identified as "others").

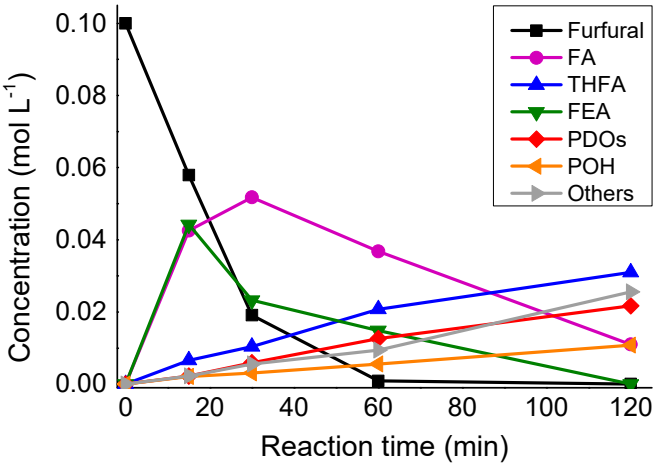

Figure 6. Furfural hydrogenation with Pt/Nb_2O_5.

The influence of the insertion of a second metal into the Nb_2O_5 structure on the catalytic performance was then investigated. $Pt/W\text{-}Nb_2O_5$ and $Pt/Ti\text{-}Nb_2O_5$ were tested in the same reaction conditions as Pt/Nb_2O_5 (50 °C and 5 bar of H_2) and the results are reported in Figure 7. Considering that Pt nanoparticles showed a similar average size (1.0–1.5 nm), any difference in catalytic activity and selectivity among the niobia-based materials can be attributed to chemical–physical properties of the various supports. The catalyst that showed the highest activity towards the hydrogenation of furfural was $Pt/W\text{-}Nb_2O_5$, with 88% of substrate being converted after only 15 min. Interestingly, this catalyst was also the one that showed the highest acidity among the series tested, with an acidity value 0.191 $mmol_{py} \cdot g_{CAT}{}^{-1}$ compared to 0.078 $mmol_{py} \cdot g_{CAT}{}^{-1}$ of Pt/Nb_2O_5 (Table 3). BET analysis revealed that both catalysts showed comparable surface areas, 95 $m^2 \cdot g^{-1}$ and 130 $m^2 \cdot g^{-1}$ respectively for Nb_2O_5 and $W\text{-}Nb_2O_5$, thus excluding any possible effect deriving from different surface areas. At the same time, the catalyst that showed the lowest value of acidity ($Pt/Ti\text{-}Nb_2O_5$, 0.014 $mmol_{py} \cdot g_{CAT}{}^{-1}$) resulted the least active of the series, with a conversion of only 23% reached after 15 min. The difference in terms of initial reaction rate is almost 4 times higher for $Pt/W\text{-}Nb_2O_5$ compared to $Pt/Ti\text{-}Nb_2O_5$ (1770 h^{-1} versus 470 h^{-1}, respectively). It is clear from these results that the acidity has a dramatic effect on the catalytic activity. We cannot exclude the presence of Meerwein–Ponndorf–Verley (MPV) reduction but in this case, FA would be present in higher amounts using a catalyst showing higher Lewis acidity, i.e., $Pt/W\text{-}Nb_2O_5$.

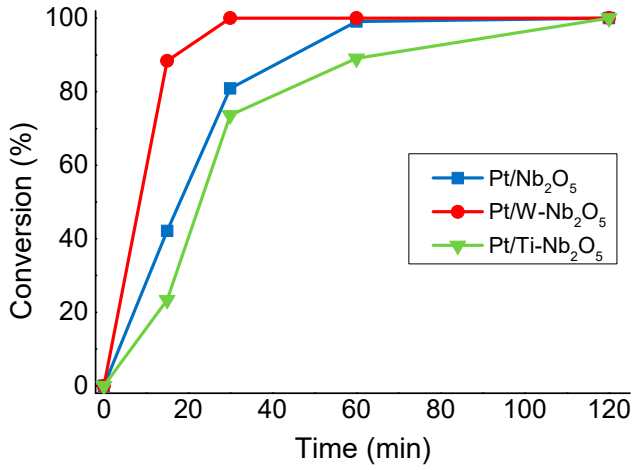

Figure 7. Furfural hydrogenation with Pt/Nb_2O_5, $Pt/W\text{-}Nb_2O_5$ and $Pt/Ti\text{-}Nb_2O_5$.

Surface acidity affected not only the activity of the catalysts, but also their selectivity although with a lower extent. Comparing the selectivity at iso-conversion (Figure 8), in fact, it is possible to notice that the selectivity to FA increased as the acidity decreased (from 50% to 61%, with Pt/W-Nb_2O_5 and Pt/Ti-Nb_2O_5, respectively). At the same time, the selectivity to FEA decreased with low acidity supports from 26% with Pt/W-Nb_2O_5 to 10% with Pt/Ti-Nb_2O_5, while the remaining reaction products did not vary significantly.

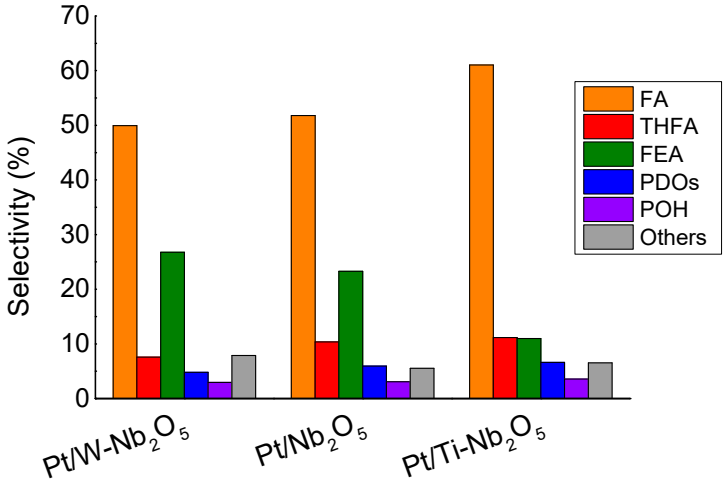

Figure 8. Product distribution of furfural hydrogenation at 90% conversion.

4. Conclusions

Niobia represents an acidic support which can be fruitfully used as supporting material for Pt nanoparticles in furfural hydrogenation, thus creating bifunctional catalyst. We found that acidity is one of the main ruling factors determining the activity in the hydrogenation of furfural, being the Pt on W-modified Nb_2O_5 the most acidic and the most active catalyst. However, the selectivity can also be strongly affected. Indeed, the W-modified niobia which showed the highest Lewis acidity produced the highest selectivity to furan-ethers. Conversely, the Pt on Ti-modified Nb_2O_5, which presents the lowest surface acidity, produces the highest selectivity to furfuryl alcohol derived most probably from Pt catalyzed hydrogenation.

Supplementary Materials: The following are available online at http://www.mdpi.com/2076-3417/9/11/2287/s1.

Author Contributions: A.J. synthesised the supports. A.J. and S.C. carried out catalytic evaluation. S.C. wrote the article. D.D. and J.M.L.N. carried out XRD, Raman and surface analysis and helped with the interpretation. N.S. carried out acidity tests and helped with the interpretation. C.E. synthesised the catalysts and carried out TEM experiments and helped with the interpretation. L.P. designed the experiments and was involved in the writing and editing of the manuscript.

Funding: This research received no external funding.

Conflicts of Interest: The authors declare no conflict of interest.

References

1. Binder, J.B.; Raines, R.T. Simple Chemical Transformation of Lignocellulosic Biomass into Furans for Fuels and Chemicals. *J. Am. Chem. Soc.* **2009**, *131*, 1879–1985. [CrossRef] [PubMed]
2. Cao, Q.; Guo, X.; Guan, J.; Mu, X.; Zhang, D. A process for efficient conversion of fructose into 5-hydroxymethylfurfural in ammonium salts. *Appl. Catal. A Gen.* **2011**, *403*, 98–103. [CrossRef]
3. Serrano-Ruiz, J.C.; Dumesic, J.A. Catalytic production of liquid hydrocarbon transportation fuels. *Catal. Altern. Energy Gener.* **2012**, *9781461403*, 29–56.
4. Cattaneo, S.; Naslhajian, H.; Somodi, F.; Evangelisti, C.; Villa, A.; Prati, L. Ruthenium on carbonaceous materials for the selective hydrogenation of HMF. *Molecules* **2018**, *23*, 2007. [CrossRef] [PubMed]

5. Qi, X.; Watanabe, M.; Aida, T.M.; Smith, R.L. Synergistic conversion of glucose into 5-hydroxymethylfurfural in ionic liquid-water mixtures. *Bioresour. Technol.* **2012**, *109*, 224–228. [CrossRef]
6. Yang, S.-T. Bioprocessing-from biotechnology to biorefinery. In *Bioprocessing for Value-Added Products from Renewable Resources*; Elsevier: Amsterdam, The Netherlands, 2007; pp. 1–24.
7. Ormsby, R.; Kastner, J.R.; Miller, J. Hemicellulose hydrolysis using solid acid catalysts generated from biochar. *Catal. Today* **2012**, *190*, 89–97. [CrossRef]
8. Lavarack, B.P.; Griffin, G.J.; Rodman, D. The acid hydrolysis of sugarcane bagasse hemicellulose to produce xylose, arabinose, glucose and other products. *Biomass Bioenergy* **2002**, *23*, 367–380. [CrossRef]
9. Carà, P.D.; Pagliaro, M.; Elmekawy, A.; Brown, D.R.; Verschuren, P.; Shiju, N.R.; Rothenberg, G. Hemicellulose hydrolysis catalysed by solid acids. *Catal. Sci. Technol.* **2013**, *3*, 2057–2061. [CrossRef]
10. O'Neill, R.; Ahmad, M.N.; Vanoye, L.; Aiouache, F. Kinetics of Aqueous Phase Dehydration of Xylose into Furfural Catalyzed by ZSM-5 Zeolite. *Ind. Eng. Chem. Res.* **2009**, *48*, 4300–4306. [CrossRef]
11. Weingarten, R.; Cho, J.; Conner, W.C., Jr.; Huber, G.W. Kinetics of furfural production by dehydration of xylose in a biphasic reactor with microwave heating. *Green Chem.* **2010**, *12*, 1423–1429. [CrossRef]
12. Gómez Bernal, H.; Bernazzani, L.; Raspolli Galletti, A.M. Furfural from corn stover hemicelluloses. A mineral acid-free approach. *Green Chem.* **2014**, *16*, 3734–3740. [CrossRef]
13. Delbecq, F.; Wang, Y.; Muralidhara, A.; El Ouardi, K.; Marlair, G.; Len, C. Hydrolysis of Hemicellulose and Derivatives—A Review of Recent Advances in the Production of Furfural. *Front. Chem.* **2018**, *6*, 146. [CrossRef]
14. Mariscal, R.; Maireles-Torres, P.; Ojeda, M.; Sádaba, I.; López Granados, M. Furfural: A renewable and versatile platform molecule for the synthesis of chemicals and fuels. *Energy Environ. Sci.* **2016**, *9*, 1144–1189. [CrossRef]
15. Yan, K.; Wu, G.; Lafleur, T.; Jarvis, C. Production, properties and catalytic hydrogenation of furfural to fuel additives and value-added chemicals. *Renew. Sustain. Energy Rev.* **2014**, *38*, 663–676. [CrossRef]
16. Bui, L.; Luo, H.; Gunther, W.R.; Román-Leshkov, Y. Domino Reaction Catalyzed by Zeolites with Brønsted and Lewis Acid Sites for the Production of γ-Valerolactone from Furfural. *Angew. Chem. Int. Ed.* **2013**, *52*, 8022–8025. [CrossRef]
17. Taylor, M.J.; Durndell, L.J.; Isaacs, M.A.; Parlett, C.M.A.; Wilson, K.; Lee, A.F.; Kyriakou, G. Highly selective hydrogenation of furfural over supported Pt nanoparticles under mild conditions. *Appl. Catal. B Environ.* **2016**, *180*, 580–585. [CrossRef]
18. Schäfer, H.; Gruen, R.; Schulte, F. The modification of niobium pentoxide. *Angew. Chem. Int. Ed.* **1996**, *5*, 40–52.
19. Allpress, J.G.; Sanders, J.V.; Wadsley, A.D. Electron Microscopy of high-temperature Nb_2O_5 and related phases. *Phys. Stat. Sol.* **1968**, *25*, 541–550. [CrossRef]
20. Jehng, J.-M.; Wachs, I.E. The molecular structures and reactivity of supported niobium oxide catalysts. *Catal. Today* **1990**, *8*, 37–55. [CrossRef]
21. Jehng, J.M.; Wachs, I.E. Molecular structures of supported niobium oxide catalysts under in situ conditions. *J. Phys. Chem.* **1991**, *95*, 7373–7379. [CrossRef]
22. Carniti, P.; Gervasini, A.; Marzo, M. Silica-niobia oxides as viable acid catalysts in water: Effective vs. intrinsic acidity. *Catal. Today* **2010**, *152*, 42–47. [CrossRef]
23. Gupta, N.K.; Fukuoka, A.; Nakajima, K. Amorphous Nb_2O_5 as a Selective and Reusable Catalyst for Furfural Production from Xylose in Biphasic Water and Toluene. *ACS Catal.* **2017**, *7*, 2430–2436. [CrossRef]
24. Marzo, M.; Gervasini, A.; Carniti, P. Improving stability of Nb_2O_5 catalyst in fructose dehydration reaction in water solvent by ion-doping. *Catal. Today* **2012**, *192*, 89–95. [CrossRef]
25. Carniti, P.; Gervasini, A.; Biella, S.; Auroux, A. Niobic acid and niobium phosphate as highly acidic viable catalysts in aqueous medium: Fructose dehydration reaction. *Catal. Today* **2006**, *118*, 373–378. [CrossRef]
26. Omata, K.; Izumi, S.; Murayama, T.; Ueda, W. Hydrothermal synthesis of W–Nb complex metal oxides and their application to catalytic dehydration of glycerol to acrolein. *Catal. Today* **2013**, *201*, 7–11. [CrossRef]
27. García-Sancho, C.; Cecilia, J.A.; Moreno-Ruiz, A.; Mérida-Robles, J.M.; Santamaría-González, J.; Moreno-Tost, R.; Maireles-Torres, P. Influence of the niobium supported species on the catalytic dehydration of glycerol to acrolein. *Appl. Catal. B Environ.* **2015**, *179*, 139–149. [CrossRef]

28. Silva, Â.; Wilson, K.; Lee, A.F.; dos Santos, V.C.; Cons Bacilla, A.C.; Mantovani, K.M.; Nakagaki, S. Nb_2O5/SBA-15 catalyzed propanoic acid esterification. *Appl. Catal. B Environ.* **2017**, *205*, 498–504. [CrossRef]
29. Noronha, F.B.; Aranda, D.A.G.; Ordine, A.P.; Schmal, M. The promoting effect of Nb_2 addition to Pd/Al_2O_3 catalysts on propane oxidation. *Catal. Today* **2000**, *57*, 275–282. [CrossRef]
30. Molina, M.J.C.; Granados, M.L.; Gervasini, A.; Carniti, P. Exploitment of niobium oxide effective acidity for xylose dehydration to furfural. *Catal. Today* **2015**, *254*, 90–98. [CrossRef]
31. Stošić, D.; Bennici, S.; Rakić, V.; Auroux, A. CeO_2-Nb_2O_5 mixed oxide catalysts: Preparation, characterization and catalytic activity in fructose dehydration reaction. *Catal. Today* **2012**, *192*, 160–168. [CrossRef]
32. Stošić, D.; Bennici, S.; Pavlović, V.; Rakić, V.; Auroux, A. Tuning the acidity of niobia: Characterization and catalytic activity of Nb_2O_5-MeO_2 (Me = Ti, Zr, Ce) mesoporous mixed oxides. *Mater. Chem. Phys.* **2014**, *146*, 337–345. [CrossRef]
33. Li, H.; Fang, Z.; Smith, R.L.; Yang, S. Efficient valorization of biomass to biofuels with bifunctional solid catalytic materials. *Prog. Energy Combust. Sci.* **2016**, *55*, 98–194. [CrossRef]
34. Coq, B. *Metal-Support Interaction In Catalysis in Metal-Ligand Interactions in Chemistry, Physics and Biology*; Russo, N., Salahub, D.R., Eds.; Springer Netherlands: Dordrecht, The Netherlands, 2000; ISBN 978-94-011-4245-8.
35. Evangelisti, C.; Aronica, L.A.; Botavina, M.; Martra, G.; Battocchio, C.; Polzonetti, G. Chemoselective hydrogenation of halonitroaromatics over γ-Fe_2O_3-supported platinum nanoparticles: The role of the support on their catalytic activity and selectivity. *J. Mol. Catal. A Chem.* **2013**, *366*, 288–293. [CrossRef]
36. Emeis, C.A. Determination of Integrated Molar Extinction Coefficients for Infrared Absorption Bands of Pyridine Adsorbed on Solid Acid Catalysts. *J. Catal.* **1993**, *141*, 347–354. [CrossRef]
37. Oberhauser, W.; Evangelisti, C.; Jumde, R.P.; Psaro, R.; Vizza, F.; Bevilacqua, M.; Filippi, J.; Machado, B.F.; Serp, P. Platinum on carbonaceous supports for glycerol hydrogenolysis: Support effect. *J. Catal.* **2015**, *325*, 111–117. [CrossRef]
38. Oberhauser, W.; Evangelisti, C.; Tiozzo, C.; Vizza, F.; Psaro, R. Lactic Acid from Glycerol by Ethylene-Stabilized Platinum-Nanoparticles. *ACS Catal.* **2016**, *6*, 1671–1674. [CrossRef]
39. La Salvia, N.; Delgado, D.; Ruiz-Rodríguez, L.; Nadji, L.; Massó, A.; Nieto, J.M.L. V- and Nb-containing tungsten bronzes catalysts for the aerobic transformation of ethanol and glycerol. Bulk and supported materials. *Catal. Today* **2017**, *296*, 2–9. [CrossRef]
40. Fernández-Arroyo, A.; Delgado, D.; Domine, M.E.; López-Nieto, J.M. Upgrading of oxygenated compounds present in aqueous biomass-derived feedstocks over NbOx-based catalysts. *Catal. Sci. Technol.* **2017**, *7*, 5495–5499. [CrossRef]
41. Shannon, R.D. Revised Effective Ionic Radii and Systematic Studies of Interatomie Distances in Halides and Chaleogenides. *Acta. Cryst.* **1976**, *32*, 751–767. [CrossRef]
42. Botella, P.; Solsona, B.; López Nieto, J.M.; Concepción, P.; Jordá, J.L.; Doménech-Carbó, M.T. Mo–W-containing tetragonal tungsten bronzes through isomorphic substitution of molybdenum by tungsten. *Catal. Today* **2010**, *158*, 162–169. [CrossRef]
43. Jehng, J.M.; Wachs, I.E. Structural chemistry and Raman spectra of niobium oxides. *Chem. Mater.* **1991**, *3*, 100–107. [CrossRef]
44. Delgado, D.; Fernández-Arroyo, A.; Domine, M.E.; García-González, E.; Nieto, J.M.L. W–Nb–O oxides with tunable acid properties as efficient catalysts for the transformation of biomass-derived oxygenates in aqueous systems. *Catal. Sci. Tech* **2019**, in press. [CrossRef]
45. Scotti, N.; Dangate, M.; Gervasini, A.; Evangelisti, C.; Ravasio, N.; Zaccheria, F. Unraveling the Role of Low Coordination Sites in a Cu Metal Nanoparticle: A Step toward the Selective Synthesis of Second Generation Biofuels. *ACS Catal.* **2014**, *4*, 2818–2826. [CrossRef]
46. Crépeau, G.; Montouillout, V.; Vimont, A.; Mariey, L.; Cseri, T.; Maugé, F. Nature, Structure and Strength of the Acidic Sites of Amorphous Silica Alumina: An IR and NMR Study. *J. Phys. Chem. B* **2006**, *110*, 15172–15185. [CrossRef]
47. Ravindra Reddy, C.; Nagendrappa, G.; Jai Prakash, B.S. Surface acidity study of Mn+-montmorillonite clay catalysts by FT-IR spectroscopy: Correlation with esterification activity. *Catal. Commun.* **2007**, *8*, 241–246. [CrossRef]

48. Gervasini, A.; Carniti, P.; Bossola, F.; Imparato, C.; Pernice, P.; Clayden, N.J.; Aronne, A. New Nb-P-Si ternary oxide materials and their use in heterogeneous acid catalysis. *Mol. Catal.* **2018**, *458*, 280–286. [CrossRef]
49. Carniti, P.; Gervasini, A.; Bossola, F.; Dal Santo, V. Cooperative action of Brønsted and Lewis acid sites of niobium phosphate catalysts for cellobiose conversion in water. *Appl. Catal. B Environ.* **2016**, *193*, 93–102. [CrossRef]